Kobayashi *et al. Earth, Planets and Space* (2023) 75:81
https://doi.org/10.1186/s40623-023-01838-z

Earth, Planets and Space

EXPRESS LETTER

Open Access

Rupture processes of the 2021 and 2022 Fukushima-oki earthquakes: adjacent events on the complex fault system in the subducting slab

Hiroaki Kobayashi[1*], Tetsushi Watanabe[1] and Kazuki Koketsu[2]

Abstract

The 2021 M_w 7.1 and 2022 M_w 7.4 Fukushima-oki earthquakes ruptured adjacent regions in the subducting slab, which gave us a good opportunity to better understand the rupture process of an intraslab earthquake and the fault system in a subducting slab hosting such large earthquakes. We developed source models of the two earthquakes by constructing fault models based on the distributions of relocated aftershocks and performing joint source inversion using strong motion, teleseismic and geodetic data. The results showed that the 2021 earthquake was initiated by the west-northwest dipping fault and that it then ruptured the east-southeast dipping fault. The rupture propagated to the southwest and up-dip directions. For the 2022 earthquake, the rupture primarily propagated to the north-northeast and up-dip directions on another east-southeast dipping fault, but a delayed rupture occurred around the hypocenter approximately 12 s after the rupture initiation. This was probably due to the complex fault system around the hypocenter. Our source models accurately reproduced observed data for both earthquakes, indicating that the fault geometry was appropriate. We found that the source faults of these earthquakes had similarities to faults in the outer-rise region, which suggests that the 2021 and 2022 earthquakes occurred on faults that originally formed in the outer-rise region and reactivated in the subducting slab. Such a fault system in the subducting slab was probably one of the factors that controlled the rupture processes of the two earthquakes.

Keywords Rupture process, Joint source inversion, Fukushima-oki earthquakes, Intraslab, Fault system

*Correspondence:
Hiroaki Kobayashi
kohiroak@kobori-takken.co.jp
Full list of author information is available at the end of the article

Graphical Abstract

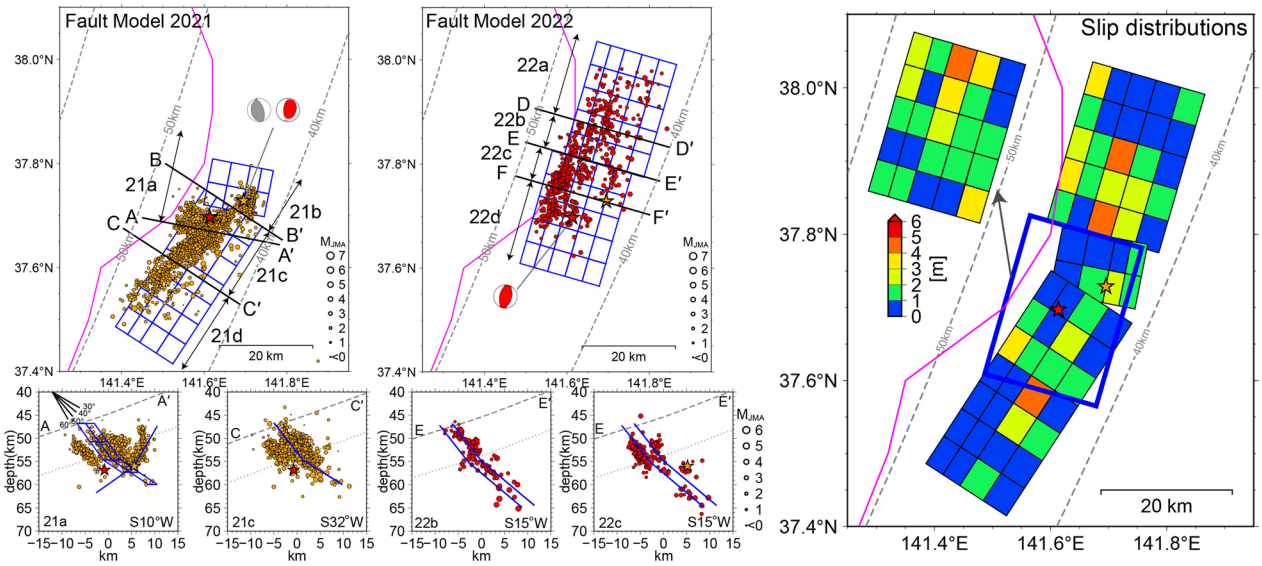

Introduction

In the Japan Trench subduction zone, the Pacific plate is converging beneath the North American plate at a rate of approximately 8.5 cm/year (Altamimi et al. 2017). At a depth of 50–200 km, the seismicity in the subducting slab forms a double-planed distribution called a double seismic zone, where the upper plane lies near the slab interface and the lower plane is in parallel with a vertical separation of 30–40 km (e.g., Hasegawa et al. 1978). The focal mechanisms indicate that the stress regimes of the upper and lower planes are down-dip compression and down-dip extension, respectively, due to the plate unbending process (Kita et al. 2010).

In northeast Japan, large intraslab earthquakes (~M 7) have occurred in both the upper (e.g., the 2003 M_w 7.0 Miyagi-oki earthquake, the 2011 M_w 7.1 Miyagi-oki earthquake) and lower planes (e.g., the 2008 M_w 6.8 Northern Iwate earthquake). On 13 February 2021 at 14:07 UTC, an earthquake with a Japan Meteorological Agency (JMA) magnitude (M_{JMA}) of 7.3 occurred in the Fukushima-oki region. Approximately 1 year later, another earthquake with an M_{JMA} of 7.4 occurred nearby on 16 March 2022 at 14:36 UTC. Although the epicenters of these earthquakes were east of the lower depth limit of the area where interplate earthquakes occur (Igarashi et al. 2001; Uchida et al. 2009), the down-dip compressional focal mechanisms and hypocenter depths (55.38 and 56.61 km in the JMA catalog) indicate that these earthquakes were intraslab events in the upper plane of the double seismic zone (Fig. 1). Moreover, the aftershock distributions suggest that these earthquakes ruptured adjacent regions in the subducting slab. Thus, they present a good opportunity to better understand the fault system in the slab that hosts such large earthquakes and the rupture process on it. Although the focal mechanisms and aftershock distributions are useful for grasping the fault geometry, source analyses are needed to confirm the fault geometry and obtain the rupture process.

In this study, we constructed a comprehensive source model of the 2021 and 2022 Fukushima-oki earthquakes by performing joint source inversions using strong motion, teleseismic and geodetic data.

Data

The strong motion data were obtained from Kyoshin Network (K-NET; National Research Institute for Earth Science and Disaster Resilience, NIED 2019), Kiban Kyoshin Network (KiK-net; NIED 2019), and JMA. We obtained velocity waveforms by integrating the original acceleration waveforms and applying a bandpass filter between 0.05 and 0.4 Hz to the integration results. We used borehole waveforms for the KiK-net stations. The teleseismic data were obtained from the Incorporated Research Institutions for Seismology Data Management Center (IRIS-DMC). We obtained displacement waveforms by deconvolving the instrumental response from the original velocity or acceleration waveform, integrating or doubly integrating the deconvolution results, and applying a

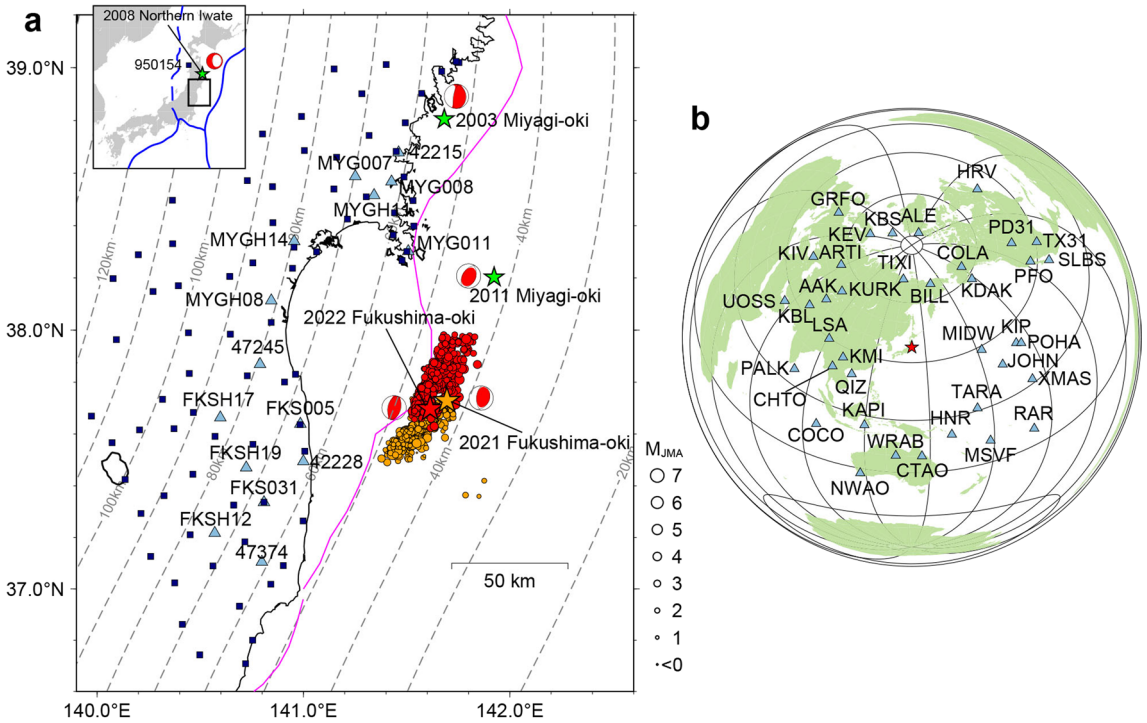

Fig. 1 **a** Seismotectonic map with the station distribution around the source region. The black rectangle in the inset represents the region shown in the larger map. The blue lines show the trench axes (Iwasaki et al. 2015), and the blue broken line indicates the boundary between the North American and Eurasian plates (Bird 2003). The orange star and circles indicate the relocated epicenters of the mainshock and 24 h aftershocks, respectively, of the 2021 Fukushima-oki earthquake, and the red star and circles indicate those for the 2022 earthquake. The green stars show the epicenters of the large intraslab earthquakes in the JMA catalog since 2000. The focal mechanisms from the catalog of the Full Range Seismograph Network of Japan (F-net; Kubo et al. 2002) are shown near the epicenters. The sky-blue triangles and dark-blue squares represent the strong motion stations and geodetic stations, respectively. The gray broken lines denote the plate-boundary depths at intervals of 10 km (Iwasaki et al. 2015). The pink lines show the lower depth limit of the area where interplate earthquakes occur (Igarashi et al. 2001; Uchida et al. 2009). **b** Distribution of teleseismic stations (sky-blue triangles). The red star represents the epicenter of the 2022 Fukushima-oki earthquake

bandpass filter between 0.01 and 0.4 Hz to the integration results. All waveforms were resampled at intervals of 0.5 s. The geodetic data were obtained from a global navigation satellite system (GNSS) of the Geospatial Information Authority of Japan (GSI). The GSI publishes the F5 solutions for the daily coordinates of GNSS Earth Observation Network System (GEONET) stations (Muramatsu et al. 2021). The geodetic data were used to calculate the coseismic displacements from difference between the 7 day averages of F5 solutions prior to and after the earthquakes. For this calculation, we adopted GEONET station 95154 (Fig. 1) as a reference. Additional file 1: Table S1 summarizes the data used in the joint source inversions.

Methods

We used a multi-time window linear inversion method (Yoshida et al. 1996; Hikima and Koketsu 2005) where a fault plane is divided into subfaults and point sources are set at the centers of each subfault. The start time of the first time window of each subfault was controlled by the rupture front velocity (V_r) at which the rupture front expands concentrically from the rupture initiation point. We used a subfault size of 5×5 km and a boxcar-type function with duration of 1 s as the basis source time function. The rake angles of two basis slip vectors were 45° and 135°. These settings were common for all analysis in this study. The strong motion, teleseismic, and geodetic datasets were jointly inverted for the lengths of slip vectors in each subfault with spatial and temporal smoothness constraints. We used a non-negative least squares method to confine the rake angles within 90±45°. The weights of the constraints were determined by minimizing Akaike's Bayesian information criterion (Akaike 1980). Because the distributions of the strong motion and geodetic stations were biased to one side when viewed from the source region (Fig. 1), the strong motion and geodetic datasets were given half the weight of the teleseismic dataset in the joint inversion analysis.

We calculated the strong motion, teleseismic, and geodetic Green's functions by using the methods of Kohketsu (1985), Kikuchi and Kanamori (1991), and Zhu

and Rivera (2002), respectively. The one-dimensional (1D) velocity structure model for each strong motion station was constructed based on the underneath velocity structure of each station extracted from the Japan Integrated Velocity Structure Model (JIVSM; Koketsu et al. 2009, 2012). We extracted Layers No. 1–17 in the JIVSM and inserted Layer No. 23 at a depth of 43 km or deeper. We also utilized PS logging data if available. Additional file 1: Tables S2 and S3 present the 1D near-source and near-receiver structures used to calculate the teleseismic Green's functions. The former was constructed from the JIVSM, and the latter was the Jeffreys–Bullen model (Bullen 1963). We used the constructed 1D structures to calculate the synthetic strong motion waveforms of two medium-size earthquakes (Events N01 and N02 in Additional file 1: Fig. S1 and Table S4) by setting point sources at the hypocenters and assuming isosceles triangle source time functions. We also calculated synthetic teleseismic waveforms of Event F01 by using the constructed 1D structures and the same settings and assumptions. Additional file 1: Figures S2–S4 compare the observed and synthetic waveforms and show that these 1D structures are appropriate. We used the 1D structure model at strong motion station MYG011 for all geodetic stations because of the lower sensitivity of the geodetic Green's function to the velocity structure model compared with the strong motion and teleseismic Green's functions.

Fault models

To obtain finer hypocenter distributions, we simultaneously relocated the hypocenters of earthquakes that occurred 13–26 February 2021 and 16–29 March 2022 by using the double-difference earthquake location method (Waldhauser and Ellsworth 2000). We used P- and S-wave arrival times that were classified as "high reliability" in the JMA catalog and JMA2001 1D velocity structure model (Ueno et al. 2002). Figure 2a–e shows the distribution of the relocated mainshock and 24-h aftershocks of the 2021 earthquake. The aftershock distribution in the subregions 21a and 21b (Fig. 2a) around the mainshock indicates a west-northwest (WNW) dipping fault plane (Fig. 2b and c) with a strike of 190° and dip angle of 35° in the lower part and 60° in the upper part. Although the lower-angle part (35°) is not clear in the aftershock distribution, we assumed it was there based on the JMA first motion solution (Fig. 2a). In subregions 21c and 21d (Fig. 2a), the aftershock distribution shows an east-southeast (ESE) dipping fault plane (Fig. 2d and e) with a strike of 32° and dip angle of 32° in the lower part and 52° in the upper part. The former dip angle is consistent with the moment tensor solutions by F-net (Kubo et al. 2002) and Global Centroid Moment Tensor (CMT) Project (Ekström et al. 2012). These fault planes are shown by blue meshes and lines in Fig. 2a–e. The WNW and ESE dipping fault planes had fault length of 10 and 35 km, respectively, and a fault width of 20 km for both. Very few aftershocks were located above the plate interface. Therefore, this earthquake was confirmed as an intraslab event, and we located the top of the fault model near the plate interface.

Figure 2f–j shows the distribution of the relocated mainshock and 24-h aftershocks of the 2022 earthquake. The aftershocks were generally distributed in the north-northeast to south-southwest directions, and they suggest an ESE dipping fault plane with a strike of 15° and dip angle of 40° in the lower part and 52° in the upper part. The dip angles of the moment tensor solutions by F-net and Global CMT Project are closer to the former dip angle. The fault is 50 km in length and 25 km in width, but the northern 25 km length is slightly shifted to the east along line EE′, which results in a stepover structure. These fault planes are shown with blue meshes and lines. Although the aftershock distribution suggests that there may be overlapping parts between the northern and southern faults (Additional file 1: Fig. S5), we did not model the overlapped fault structure for the sake of simplicity and applied the smoothness constraint continuously at the stepover structure in the inversion analyses. The top of the fault plane was determined in the same manner as for the 2021 earthquake. In both the fault models for the 2021 and 2022 earthquakes the connecting line of the lower and upper parts with different dip angles almost coincided with the surface at a depth of 8.4 km from the plate boundary (gray dotted lines in Fig. 2). Because the typical thickness of the oceanic crust in this region of the JIVSM model was 8.4 km, our fault models bent near the boundary between the oceanic crust and mantle.

Results

For the 2021 earthquake, we performed the joint source inversions with six time-windows and V_r of 1.5–4.3 km/s with intervals of 0.2 km/s. We then chose the joint source inversion with V_r of 2.9 km/s because no significant reduction of residuals occurred in the inversions with faster V_r. Figure 3 shows the results. The rupture initiation point was set at the center of the nearest subfault with the low dip angle (35°) from the hypocenter. The largest slip of 4.4 m was obtained at the center of the ESE dipping fault in the south and the second largest slip of 3.5 m was obtained at the top of the same fault (Fig. 3a). A slip of about ~ 2 m was also obtained on the WNW dipping fault in the north. Figure 3b shows that the main rupture propagated in the up-dip direction on the WNW dipping fault and along the strike and up-dip directions on the ESE dipping fault. The maximum slip

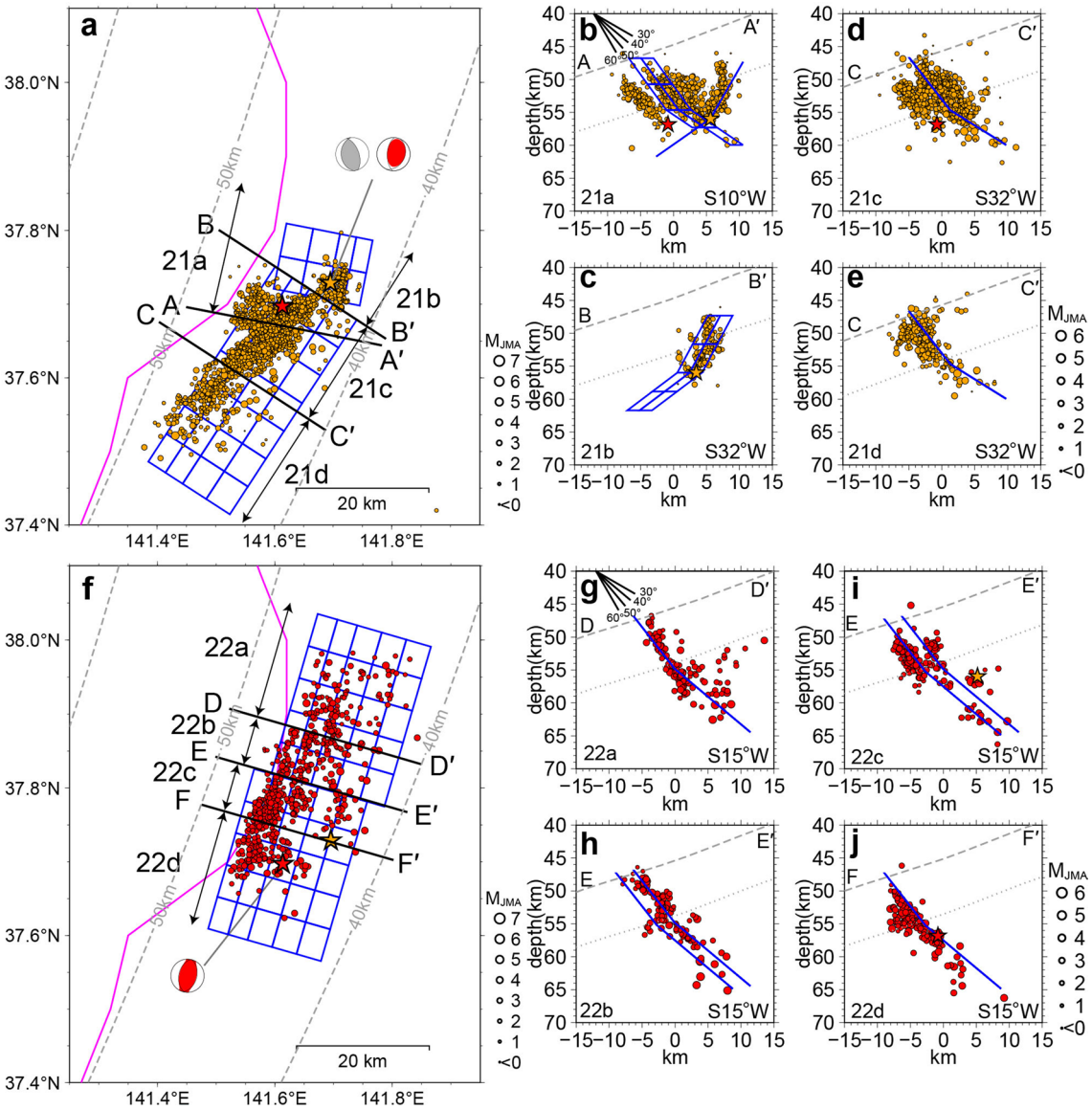

Fig. 2 **a** Fault model and relocated 24 h aftershock distribution (orange circles) for the 2021 Fukushima-oki earthquake. **b**–**e** Their cross-sections along lines AA′, BB′, and CC′ for subregions 21a, 21b, 21c, and 21d in Panel **a**. **f** Fault model and relocated 24 h aftershock distribution (red circles) for the 2022 Fukushima-oki earthquake. **g**–**j** Their cross-sections along the lines DD′, EE′, and FF′ for subregions 22a, 22b, 22c, and 22d in Panel **f**. The orange and red stars indicate the relocated epicenters of the 2021 and 2022 the mainshocks, respectively. The blue meshes and lines show the fault models. For each cross-section, the viewing direction is displayed at the lower right corner. Gray-white and red-white focal mechanisms represent the first motion solution by JMA and moment tensor solutions from the F-net catalog, respectively. The gray broken lines in Panel **a** denote the plate boundary depths as in Fig. 1. The shapes of the plate boundary along the lines in Panels **a** and **f** are shown in the cross-sections. The gray dotted lines represent the surface at a depth of 8.4 km from the plate boundary, which corresponds to the typical thickness of the oceanic crust of the Pacific plate in the JIVSM model. The pink lines show the same depth limit as in Fig. 1

(See figure on next page.)

Fig. 3 Source inversion results of the 2021 Fukushima-oki earthquake. **a** Slip distribution. The orange star represents the hypocenter of the earthquake. The black and white circles indicate the corresponding locations on the faults in Panel **c**. **b** Snapshots of the slip distribution. **c** Slip rate function of each subfault. **d** Apparent moment rate function. **e**, **f** Observed (black) and synthetic (red) strong motion velocity waveforms (0.05–0.4 Hz) and teleseismic displacement waveforms (0.01–0.4 Hz). The station name, component, maximum observed amplitude (cm/s for strong motion and μm for teleseismic) are shown to the left of each waveform. **g** Observed (black) and synthetic (red) horizontal static displacements

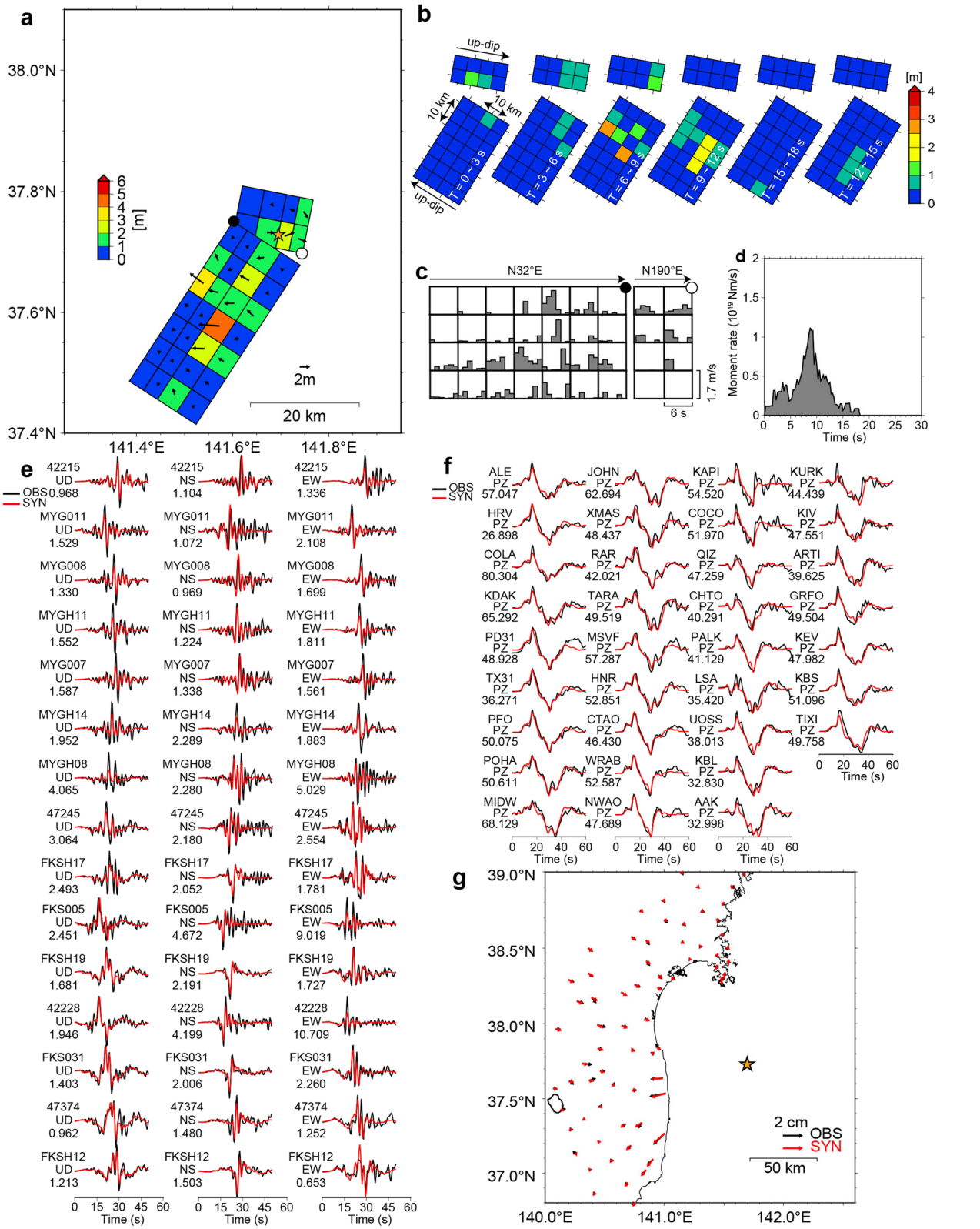

Fig. 3 (See legend on previous page.)

rates were around the large slip areas on the ESE dipping fault (Fig. 3c). The apparent moment rate function (Fig. 3d) indicates that the moment release was relatively small in the first 5 s and then peaked around 9 s, which corresponds to the large slips on the ESE dipping fault (third and fourth snapshots in Figs. 3b). The total seismic moment was estimated to be 6.1×10^{19} Nm, which corresponds to a moment magnitude (M_w) of 7.1. The observed data were accurately reproduced by the synthetic data for all datasets (Fig. 3e–g).

Figure 4 shows the results of the joint source inversion of the 2022 earthquake. We used 12 time windows and determined V_r as 2.5 km/s similar to the manner we selected V_r for the 2021 earthquake. Slips greater than 4 m were obtained in the central and northern parts of the whole source fault (Fig. 4a). The rupture propagated along the strike and up-dip directions (Fig. 4b). However, approximately 12 s after the rupture initiation, the subfaults around the hypocenter were ruptured (fifth snapshot of Fig. 4b). Figure 4c indicates that the maximum slip rates were in the large slip areas, similar to Fig. 3c. The apparent moment rate function (Fig. 4d) shows that the moment release was relatively small in the first 4 s, after which there were multiple peaks. The total seismic moment was estimated to be 1.4×10^{20} Nm, which corresponds to an M_w of 7.4. The observed data were accurately reproduced by the synthetic data except at geodetic station 960549 (Fig. 4e–g). Because the static displacements at other stations around station 960549 were reproduced well, this may be because station 960549 was affected by local deformation.

Discussion and conclusions

A subparallel ESE dipping fault can be observed in Fig. 2b and d. Thus, we performed an additional joint source inversion for the 2021 earthquake with another fault model that included the subparallel fault (Additional file 1: Fig. S6). Because the aftershocks of the 2021 earthquake indicating this subparallel fault were located in the region where we already constructed the fault model for the 2022 earthquake, the subparallel fault was derived from the fault model of the 2022 earthquake. The results of the additional inversion showed that slips greater than 1 m were obtained on the subparallel fault (Additional file 1: Fig. S7). However, the introduction of the subparallel fault reduced the variance by only 5%, so we chose the fault model without it as a preferred model.

We used 12 time windows for the joint source inversion of the 2022 earthquake (Fig. 4), which was twice the number used for the 2021 earthquake. We needed such many time windows to express the delayed rupture around the hypocenter (Fig. 4b). Additional file 1: Figure S8 shows the results of the joint source inversion with six time windows when the other parameters were kept the same. Although the teleseismic waveforms were still reproduced well (Additional file 1: Fig. S8f), the fitting of the strong motion waveforms of station 47,245 to station FKSH12 west of the source region (Fig. 1) was clearly worse, especially at the phases indicated by the blue lines in Additional file 1: Fig. S8e. The fit of the geodetic data also worsened west of the source region (Additional file 1: Fig. S8g). In total, the variance increased by 28%.

The 2021 earthquake was initiated by the WNW dipping fault and then ruptured the ESE dipping fault. The hypocenter of the 2022 earthquake was on another ESE dipping fault and the rupture primarily propagated to the north-northeast and up-dip directions beyond the stepover structure. Around the hypocenter of the 2022 earthquake, the delayed rupture occurred. Figure 5 shows the two- and three-dimensional views of the slip distributions of the 2021 and 2022 earthquakes. There are two common features in the rupture processes of the 2021 and 2022 earthquakes. First, the moment release was relatively small in the first several seconds and then peaked (Figs. 3d and 4d). Second, the slips greater than 4 m were obtained on the lower parts of the faults (Fig. 5). The former indicates the cascading rupture over the multiple faults and the latter indicates that the stress was primarily accumulated in the uppermost part of the oceanic mantle in the subducting slab. Note that the slips greater than 4 m of the two earthquakes were spatially separated and located in areas with relatively few aftershocks (Additional file 1: Fig. S9). As shown in Fig. 5, the fault system is so complex that the faults bend and both WNW dipping and ESE dipping faults exist. We suggest that this complex fault system may have caused the delayed rupture during the 2022 earthquake.

Our source models accurately reproduced observed data for both earthquakes and it suggested that the fault geometry was appropriate. Other studies have proposed that intraslab earthquakes occur on faults that form in the outer-rise region before subducting (Silver et al. 1995; Jiao et al. 2000; Ranore et al. 2005). According to recent marine surveys in the outer-rise region

(See figure on next page.)

Fig. 4 Source inversion results of the 2022 Fukushima-oki earthquake. **a** Slip distribution. The red star represents the hypocenter of the earthquake. The black circle indicates the corresponding locations on the fault in Panel **c**. **b** Snapshots of the slip distribution. **c** Slip rate function of each subfault. **d** Apparent moment rate function. **e**, **f** Observed (black) and synthetic (red) strong motion velocity waveforms (0.05–0.4 Hz) and teleseismic displacement waveforms (0.01–0.4 Hz). The station name, component, maximum observed amplitude (cm/s for strong motion and μm for teleseismic) are shown to the left of each waveform. **g** Observed (black) and synthetic (red) horizontal static displacements

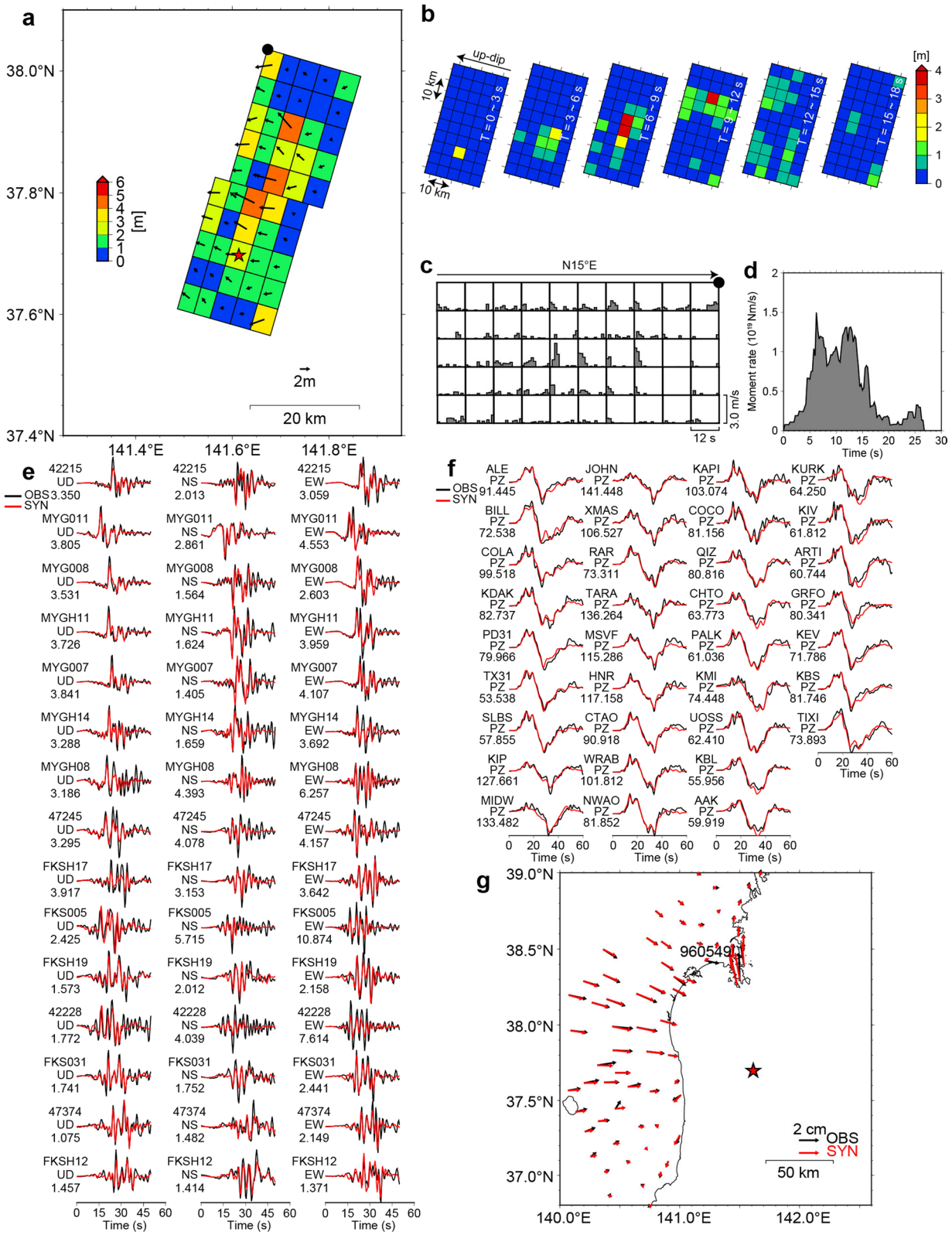

Fig. 4 (See legend on previous page.)

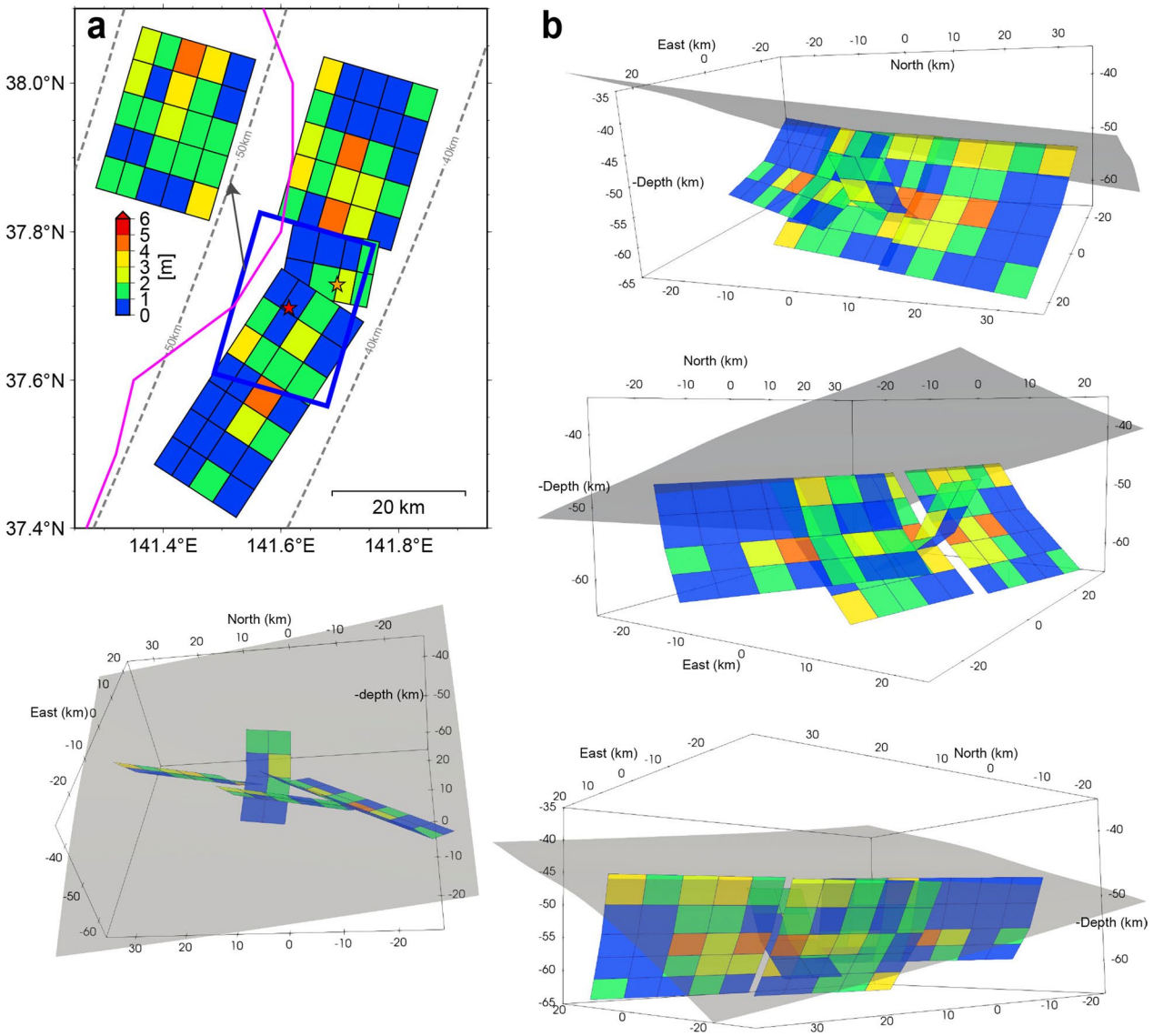

Fig. 5 Slip distributions of the 2021 and 2022 Fukushima-oki earthquakes. **a** Two-dimensional view. The slip distribution on the fault (thick blue square) is drawn on the left. The orange and red stars indicate the relocated epicenters of the 2021 and 2022 mainshocks, respectively. The gray broken lines indicate the plate-boundary depth at intervals of 10 km (Iwasaki et al. 2015). The pink line shows the same depth limit as in Fig. 1. **b** Three-dimensional views. The grey surface represents the plate-boundary

of the Japan Trench (Boston et al. 2014; Kodaira et al. 2017; Obana et al. 2018; Baba et al. 2020), there are many landward and seaward dipping faults along the trench strike whose dip angles are up to 75° near the surface and 45–60° at deeper depths. These faults are situated adjacent to each other, and they show a complex fault system in the outer-rise region. The source faults of the 2021 and 2022 earthquakes are also along the trench strike and consist of both landward and seaward dipping faults. Moreover, because the dip angle of the plate boundary is approximately 20° around the source region of the 2021 and 2022 earthquakes (Figs. 2, 5), the angle between the plate boundary and our fault models is 72° near the plate boundary and are 40–62° at depths below the hypocenters, except for the unclear low-angle WNW dipping fault around the hypocenter of the 2021 earthquake. These dip angles are consistent with the dip angles of the outer-rise faults. These similarities indicate that the source faults of the 2021 and 2022 earthquakes originally formed in the outer-rise region and reactivated in the subducting slab. The same has been suggested for the 2003 M_w 7.0 and the 2011

M_w 7.1 Miyagi-oki earthquakes based on fault modeling using geodetic data or seismic tomography and aftershock distributions (Nakajima et al. 2011; Ohta et al. 2011). Moreover, Wang et al. (2022) recently performed seismic tomography in the Fukushima-oki and Miyagi-oki regions using both onshore and offshore stations. They found that the four large intraslab earthquakes in the region occurred in relatively low-V_p areas between high-V_p areas, and they suggested that the earthquakes occurred due to dehydration embrittlement on faults that formed in the outer-rise region. These studies support our suggestion on the Fukushima-oki earthquakes.

Because faults in the outer-rise region reach a depth of 40 km from the surface and many faults are mapped over 300 km along the trench (e.g., Baba et al. 2020), a similar fault system may exist outside the combined source region of the Fukushima-oki earthquakes. In the Japan Trench subduction zone, a neutral plane lies between the planes of the double seismic zone at a depth of 22 km from the plate boundary (Kita et al. 2010). This may control the rupture extension in the depth direction. In the horizontal direction, the heterogeneous velocity structures in the subduction zone (Nakajima et al. 2011; Wang et al. 2022) and fault distribution in the outer-rise region may provide possible candidates for future source faults.

We performed joint source inversions using strong motion, teleseismic, and geodetic data to investigate the rupture processes of the 2021 and 2022 Fukushima-oki earthquakes. Fault models of the two earthquakes were constructed based on the relocated aftershock distributions. The results showed that, for the 2021 earthquake, the rupture started on the WNW dipping fault and propagated along the up-dip and strike directions for both the WNW and ESE dipping faults. For the 2022 earthquake, the rupture primarily propagated along the strike and up-dip directions. However, a delayed rupture occurred around the hypocenter approximately 12 s after rupture initiation, which was probably due to the complex fault structure around the hypocenter. Synthetic data computed with our models accurately reproduced the observed data for both earthquakes and it indicates the appropriateness of the fault geometry. The angles between the plate boundary and our fault models were consistent with the dip angles of faults in the outer-rise region. Moreover, the complex fault system in the source region was also consistent with the fault distribution in the outer-rise region. These similarities suggested that the 2021 and 2022 earthquakes occurred on faults that originally formed in the outer-rise region and reactivated in the subducting slab. Such a fault system in the subducting slab probably partly controlled the rupture processes of the two earthquakes.

Abbreviations

1D	One-dimensional
CMT	Centroid moment tensor
ESE	East-southeast
F-net	Full Range Seismograph Network of Japan
GEONET	GNSS Earth Observation Network System
GNSS	Global Navigation Satellite System
GSI	Geospatial Information Authority of Japan
IRIS-DMC	Incorporated Research Institutions for Seismology Data Management Center
JIVSM	Japan Integrated Velocity Structure Model
JMA	Japan Meteorological Agency
K-NET	Kyoshin Network
KiK-net	Kiban Kyoshin Network
NIED	National Research Institute for Earth Science and Disaster Resilience
WNW	West-northwest

Supplementary Information

The online version contains supplementary material available at https://doi.org/10.1186/s40623-023-01838-z.

Additional file 1: Contains **Figures S1–S9** and **Tables S1–S3**.

Acknowledgements
We thank two anonymous reviewers for their helpful comments. Most of the figures were drawn by using General Mapping Tools (Wessel et al. 2013). The plate models of Iwasaki T et al. (2015) were constructed from topography and bathymetry data by the Geospatial Information Authority of Japan (250 m digital map), Japan Oceanographic Data Center (500 m mesh bathymetry data, J-EGG500, http://www.jodc.go.jp/jodcweb/JDOSS/infoJEGG_j.html) and Geographic Information Network of Alaska, University of Alaska (Lindquist et al. 2004).

Author contributions
HK conducted the analysis. TW and KK participated in the discussion and the interpretation of the results. All authors drafted the manuscript. All authors read and approved the final manuscript.

Funding
No funding was received.

Availability of data and materials
The K-NET, KiK-net, and JMA strong motion waveforms are available at their websites (https://www.kyoshin.bosai.go.jp/ and https://www.data.jma.go.jp/eew/data/ltpgm_explain/data/past/past_list.html, in Japanese). The teleseismic waveforms are available from the IRIS-DMC Wilber 3 system (https://ds.iris.edu/wilber3/find_event). The GEONET F5 solution is available at the GSI website (https://www.gsi.go.jp/ENGLISH/geonet_english.html). The JMA catalog is available at the Hi-net website (https://www.hinet.bosai.go.jp/?LANG=en). The JIVSM is available at https://www.jishin.go.jp/evaluation/seismic_hazard_map/lpshm/12_choshuki_dat/ (in Japanese). The plate model of Iwasaki et al. (2015) is available at http://evrrss.eri.u-tokyo.ac.jp/database/PLATEmodel/ (in Japanese). The depth limit data of interplate earthquakes on the Pacific plate of Igarashi et al. (2001) and Uchida et al. (2009) are available at Uchida's website (https://www.aob.gp.tohoku.ac.jp/~uchida/indexe.html).

Declarations

Ethics approval and consent to participate
Not applicable.

Consent for publication
Not applicable.

Competing interests
The authors declare that they have no competing interests.

Author details
[1]Kobori Research Complex Inc., 6-5-30 Akasaka, Minato-ku, Tokyo, Japan. [2]Graduate School of Media and Governance, Keio University, 5322 Endo, Fujisawa-shi, Kanagawa, Japan.

Received: 22 December 2022 Accepted: 28 April 2023
Published online: 15 May 2023

References

Akaike H (1980) Likelihood and the Bayes procedure. Trabajos De Estadisticay De Investigacion Operativa 31:143–166. https://doi.org/10.1007/BF02888350

Altamimi Z, Métivier L, Rebischung P, Rouby H, Collilieux X (2017) ITRF2014 plate motion model. Geophys J Int 209:1906–1912. https://doi.org/10.1093/gji/ggx136

Baba T, Chikasada N, Nakamura Y, Fujie G, Obana K, Miura S, Kodaira S (2020) Deep investigations of outer-rise tsunami characteristics using well-mapped normal faults along the Japan Trench. J Geophys Res Solid Earth. https://doi.org/10.1029/2020JB020060

Bird P (2003) An updated digital model of plate boundaries. Geochem Geophys Geosyst 4:1027. https://doi.org/10.1029/2001GC000252

Boston B, Moore GF, Nakamura Y, Kodaira S (2014) Outer-rise normal fault development and influence on near-trench décollement propagation along the Japan Trench, off Tohoku. Earth Planet Space 66:135. https://doi.org/10.1186/1880-5981-66-135

Bullen KE (1963) An introduction to the theory of seismology. Cambridge University Press, New York

Ekström G, Nettles M, Dziewonski AM (2012) The global CMT project 2004–2010: centroid-moment tensors for 13,017 earthquakes. Phys Earth Planet Inter 200–201:1–9. https://doi.org/10.1016/j.pepi.2012.04.002

Hasegawa A, Umino N, Takagi A (1978) Double-planed structure of the deep seismic zone in the northeastern Japan arc. Tectonophysics 47:43–58. https://doi.org/10.1016/0040-1951(78)90150-6

Hikima K, Koketsu K (2005) Rupture processes of the 2004 Chuetsu (mid-Niigata prefecture) earthquake, Japan: a series of events in a complex fault system. Geophys Res Lett 32:L18303. https://doi.org/10.1029/2005GL023588

Igarashi T, Matsuzawa T, Umino N, Hasegawa A (2001) Spatial distribution of focal mechanisms for interplate and intraplate earthquakes associated with the subducting Pacific plate beneath the northeastern Japan arc: a triple-planed deep seismic zone. J Geophys Res 106:2177–2191. https://doi.org/10.1029/2000JB900386

Iwasaki T, Sato H, Shinohara M, Ishiyama T, Hashima A (2015). Fundamental structure model of island arcs and subducted plates in and around Japan. Paper presented at 2015 Fall Meeting American Geophysical Union San Francisco. 14 18

Jiao W, Silver PG, Fei Y, Prewitt CT (2000) Do intermediate- and deep-focus earthquakes occur on preexisting weak zones? An examination of the Tonga subduction zone. J Geophys Res 105:28125–28138. https://doi.org/10.1029/2000JB900314

Kikuchi M, Kanamori H (1991) Inversion of complex body waves—III. Bull Seismol Soc Am 81:2335–2350. https://doi.org/10.1785/BSSA0810062335

Kita S, Okada T, Hasegawa A, Nakajima J, Matsuzawa T (2010) Existence of interplane earthquakes and neutral stress boundary between the upper and lower planes of the double seismic zone beneath Tohoku and Hokkaido, northeastern Japan. Tectonophysics 496:68–82. https://doi.org/10.1016/j.tecto.2010.10.010

Kodaira S, Nakamura Y, Yamamoto Y, Obana K, Fujie G, No T, Kaiho Y, Sato T, Miura S (2017) Depth-varying structural characters in the rupture zone of the 2011 Tohoku-oki earthquake. Geosphere 13:1408–1424. https://doi.org/10.1130/GES01489.1

Kohketsu K (1985) The extended reflectivity method for synthetic near-field seismograms J Phys. Earth 33:121–131. https://doi.org/10.4294/jpe1952.33.121

Koketsu K, Miyake H, Afnimar TY (2009) A proposal for a standard procedure of modeling 3-D velocity structures and its application to the Tokyo metropolitan area, Japan. Tectonophysics 472:290–300. https://doi.org/10.1016/j.tecto.2008.05.037

Koketsu K, Miyake H, Suzuki H (2012) Japan integrated velocity structure model version 1. In: Proceedings of the 15th world conference on earthquake engineering, Lisbon. Portugal. 24–28 Sept.

Kubo A, Fukuyama E, Kawai H, Nonomura K (2002) NIED seismic moment tensor catalogue for regional earthquakes around Japan: quality test and application. Tectonophysics 356:23–48. https://doi.org/10.1016/S0040-1951(02)00375-X

Lindquist KG, Engle K, Stahlke D, Price E (2004) Global topography and bathymetry grid improves research efforts. EOS Trans Am Geophys Union 85:186. https://doi.org/10.1029/2004EO190003

Muramatsu H, Takamatsu N, Abe S, Furuya T, Kato C, Ohno K, Hayanaka Y, Kakiage Y, Ohashi K (2021) Updating daily solution of CORS in Japan using new GEONET 5th analysis strategy. J Geospatial Info Auth 134:19–32

Nakajima J, Hasegawa A, Kita S (2011) Seismic evidence for reactivation of a buried hydrated fault in the Pacific slab by the 2011 M9 0 Tohoku earthquake. Geophys Res Lett. https://doi.org/10.1029/2011GL048432

NIED (2019) NIED K-NET, KiK-net. https://doi.org/10.17598/nied.0004

Obana K, Nakamura Y, Fujie G, Kodaira S, Kaiho Y, Yamamoto Y, Miura S (2018) Seismicity in the source areas of the 1896 and 1933 Sanriku earthquakes and implications for large near-trench earthquake faults. Geophys J Int 212:2061–2072. https://doi.org/10.1093/gji/ggx532

Ohta Y, Miura S, Ohzono M, Kita S, Iinuma T, Demachi T, Tachibana K, Nakayama T, Hirahara S, Suzuki S, Sato T, Uchida N, Hasegawa A, Umino N (2011) Large intraslab earthquake (2011 April 7, M 7.1) after the 2011 off the Pacific coast of Tohoku Earthquake (M 9.0): Coseismic fault model based on the dense GPS network data. Earth Planet Space 63:1207–1211. https://doi.org/10.5047/eps.2011.07.016

Ranore CR, Villaseñor A, Morgan JP, Weinrebe W (2005) Relationship between bend-faulting at trenches and intermediate-depth seismicity. Geochem Geophys Geosyst 6:Q12002. https://doi.org/10.1029/2005GC000997

Silver PG, Beck SL, Wallace TC, Meade C, Myers SC, James DE, Kuehnel R (1995) Rupture characteristics of the deep Bolivian earthquake of 9 june 1994 and the mechanism of deep-focus earthquakes. Science 268:69–73. https://doi.org/10.1126/science.268.5207.69

Uchida N, Nakajima J, Hasegawa A, Matsuzawa T (2009) What controls interplate coupling?: Evidence for abrupt change in coupling across a border between two overlying plates in the NE Japan subduction zone. Earth Planet Sci Lett 283:111–121. https://doi.org/10.1016/j.epsl.2009.04.003

Ueno H, Hatakeyama S, Aketagawa T, Funasaki J, Hamada N (2002) Improvement of hypocenter determination procedures in the Japan meteorological agency. Q J Seismol 65:123–134

Waldhauser F, Ellsworth WL (2000) A double-difference earthquake location algorithm: method and application to the Northern Hayward Fault, California. Bull Seismol Soc Am 90:1353–1368. https://doi.org/10.1785/0120000006

Wang Z, Zhao D, Chen X (2022) Fine structure of the subducting slab and the 2022 M 7 4 Fukushima-Oki Intraslab Earthquake. Seismol Res Lett. https://doi.org/10.1785/0220220234

Wessel P, Smith WHF, Scharroo R, Luis J, Wobbe F (2013) Generic Mapping Tools: Improved version released. Eos Trans AGU 94:409. https://doi.org/10.1002/2013EO450001

Yoshida S, Koketsu K, Shibazaki B, Sagiya T, Kato T, Yoshida Y (1996) Joint inversion of near- and far-field waveforms and geodetic data for the rupture process of the 1995 Kobe earthquake. J Phys Earth 44:437–454. https://doi.org/10.4294/jpe1952.44.437

Zhu L, Rivera LA (2002) A note on the dynamic and static displacements from a point source in multilayered media. Geophys J Int. https://doi.org/10.1046/j.1365-246X.2002.01610.x

Publisher's Note